

MGMAR: Metal-Guided Metal Artifact Reduction for X-ray Computed Tomography

Hyoung Suk Park¹ and Kiwan Jeon¹

¹National Institute for Mathematical Sciences, Daejeon, 34047, Republic of Korea

Correspondence: Kiwan Jeon Email: jeonkiwan@nims.re.kr

Abstract

In X-ray computed tomography (CT), metal artifact reduction (MAR) remains a major challenge because metallic implants violate standard CT forward-model assumptions, producing severe streaking and shadowing artifacts that degrade diagnostic quality. We propose MGMAR, a metal-guided MAR method that explicitly leverages metal-related information throughout the reconstruction pipeline. MGMAR first generates a high-quality prior image by training a conditioned implicit neural representation (INR) using metal-unaffected projections, and then incorporates this prior into a normalized MAR (NMAR) framework for projection completion. To improve robustness under severe metal corruption, we pretrain the encoder-conditioned INR on paired metal-corrupted and artifact-free CT images, thereby embedding data-driven prior knowledge into the INR parameter space. This prior-embedded initialization reduces sensitivity to random initialization and accelerates convergence during measurement-specific refinement. The encoder takes a metal-corrupted reconstruction together with a recursively constructed metal artifact image, enabling the latent field to capture metal-dependent global artifact patterns. After projection completion using the INR prior, we further suppress residual artifacts using a metal-conditioned correction network, where the metal mask modulates intermediate features via adaptive instance normalization to target metal-dependent secondary artifacts while preserving anatomical structures. Experiments on the public AAPM-MAR benchmark demonstrate that MGMAR achieves state-of-the-art performance, attaining an average final score of 0.89 on 29 clinical test cases.

I. Introduction

X-ray computed tomography (CT) is widely utilized across a broad range of clinical applications, including diagnostic imaging, treatment planning, and image-guided interventions^{1,2}. However, the presence of metallic implants, such as hip prostheses, dental fillings, and spinal screws, severely violates the linear attenuation assumption underlying the filtered back-projection (FBP) algorithm³, giving rise to a highly nonlinear and ill-posed reconstruction problem⁴. These violations are primarily attributed to several physical phenomena, including beam hardening, scattering, nonlinear partial volume effects, and photon starvation. Consequently, metal artifacts, typically manifested as streaking and shadowing in reconstructed images, significantly degrade diagnostic quality and hinder reliable clinical interpretation¹. As metallic implants are increasingly used in clinical practice, the demand for effective metal artifact reduction (MAR) techniques has become increasingly critical.

Over the past decades, numerous MAR approaches have been proposed, including projection-completion methods^{5,6,7,8,9,10,11} and model-based reconstruction methods^{12,13,14,15,16,17}. Projection completion methods typically attempt to restore metal-corrupted sinogram regions through interpolation-based inpainting. To facilitate more accurate interpolation, these methods often normalize the sinogram using a prior image that is obtained via multi-threshold tissue classification (air, soft tissue, bone)^{8,18,19}. Although the normalized MAR (NMAR) framework has demonstrated improved robustness, its performance heavily depends on the accuracy and consistency of the prior image^{1,20}.

Model-based reconstruction methods aim to estimate energy-independent quantities (e.g., density or monochromatic images) by explicitly modeling the polychromatic X-ray acquisition process, thereby mitigating metal-induced beam hardening effects. Statistical iterative reconstruction techniques update the desired image by maximizing the log-likelihood of the measurements under a polychromatic forward model, often combined with hand-crafted priors such as edge-preserving regularization¹³. However, these methods require detailed prior knowledge of the X-ray spectrum and material-dependent attenuation coefficients, and they typically entail substantial computational burden. A metal-induced beam hardening correction formula has been proposed to mitigate nonlinear beam-hardening effects²¹, yet it remains limited in addressing interactions between metal and other highly attenuating structures such as bone or teeth.

The performance of existing MAR methods has been further enhanced through the integration of deep learning. Projection completion approaches have benefited from learning-based prior image generation, enabling more accurate sinogram restoration and artifact suppression^{1,22,23}. Deep neural networks have also been employed to directly replace metal-corrupted sinogram segments through data-driven interpolation^{24,25,26}. Dual-domain frameworks enhance projection completion by coupling sinogram inpainting with image-domain constraints, thereby improving restoration of the metal-corrupted sinogram^{27,28,29}.

Implicit neural representations (INRs) have recently emerged as a promising alternative for CT image reconstruction, modeling an image as a continuous function parameterized by a multilayer perceptron (MLP)^{30,31}. This resolution-independent parameterization offers advantages over conventional grid-based representations, particularly for ill-posed CT reconstruction problems^{32,33,34,35,36}. Recent studies have incorporated a polychromatic forward model into the training objective, enabling the network to map spatial coordinates (e.g., pixel/voxel positions) to an energy-independent attenuation value^{33,37,38}. Nevertheless, such polychromatic model-based formulations may not fully address other acquisition effects, such as photon starvation and scatter.

Motivated by prior works, we propose a metal-guided MAR method (MGMAR) that explicitly incorporates metal-related information throughout the reconstruction pipeline. MGMAR first generates a high-quality prior image by training a conditioned INR using metal-unaffected projections, and subsequently integrates this prior into a normalized MAR (NMAR) framework for projection completion.

Although INRs provide an effective continuous representation for ill-posed reconstruction problems, their optimization can become unstable when metal-unaffected projections are severely limited by large or multiple metallic objects, leading to reconstructions that vary across different random initializations (see Fig. 2). To improve robustness under such conditions, we embed data-driven prior knowledge directly into the INR parameter space via pretraining-based weight initialization on paired metal-corrupted and artifact-free CT images. This prior-embedded initialization reduces sensitivity to random initialization and provides a reliable starting point for subsequent measurement-specific refinement.

To enable effective knowledge sharing across samples, we adopt an encoder-conditioned INR architecture. While previous encoder-based INR approaches map an input image to a

latent code for conditioning a shared MLP^{30,39,40}, conventional convolutional encoders are primarily driven by local receptive fields and may struggle to capture globally distributed metal artifact patterns. To address this limitation, we design an artifact-aware latent conditioning strategy in which the encoder takes both a metal-corrupted CT reconstruction and a recursively constructed metal-artifact image as inputs. This design allows the latent field to encode metal-dependent global streaking and shadowing patterns, which is critical for robust prior estimation under severe corruption. The resulting pretrained weights are used to initialize the encoder-conditioned INR, thereby embedding data-driven prior knowledge into the network and improving reconstruction quality with substantially reduced computational cost.

Following projection completion with the INR prior, we further suppress secondary artifacts introduced by imperfect interpolation using a metal-conditioned residual learning network. Specifically, the metal mask modulates intermediate feature maps through an adaptive instance normalization (AdaIN)-based operation, encouraging the network to focus on metal-dependent secondary artifacts while preserving non-metal anatomical structures.

The proposed method was evaluated on the AAPM CT Metal Artifact Reduction (AAPM-MAR) Grand Challenge dataset⁴¹, which comprises 14,000 paired simulated training cases and 29 clinical metal-corrupted test cases assessed using eight clinically relevant image-quality metrics. Our preliminary submission achieved second place in the competition, and the corresponding algorithm is summarized in the benchmark paper⁴¹. In the previous version, the prior image was generated using a meta-initialization strategy^{42,43} pretrained solely on ground-truth projections from the training dataset. In this study, we further enhance the framework by introducing the proposed data-driven prior generation strategy and simplifying the overall pipeline by removing a redundant NMAR step. The improved version achieves state-of-the-art performance, attaining an average final score of 0.89 on the 29 clinical test cases.

Our contributions include: (i) A metal-guided MAR framework that explicitly integrates metal-related information throughout the reconstruction pipeline; (ii) A data-driven weight initialization strategy based on metal artifact-aware latent conditioning, which substantially improves training stability, reconstruction quality, and computational efficiency; (iii) A metal-embedded residual learning network that effectively suppresses secondary arti-

facts caused by inaccurate projection-completion; (iv) State-of-the-art performance on the AAPM-MAR dataset across clinically relevant image-quality metrics.

II. Method

We consider a 2D fan-beam CT acquisition geometry with a curved detector, where a fan-shaped X-ray beam traverses the patient’s head or body and is recorded at discrete detector bins. Let $P(\varphi, s)$ denote the metal-corrupted projection data, where $\varphi \in [0, 2\pi)$ represents the projection angle and $s \in \mathbb{R}$ denotes the detector position along the curved detector. Given P , the conventional FBP reconstructs a CT image $\mu(\mathbf{x}) = \mathcal{B}[P](\mathbf{x})$, where $\mathbf{x} \in \Omega$ denotes a spatial position in the image domain Ω and $\mathcal{B}[\cdot]$ represents the FBP operator³.

In the presence of metallic implants in the patient, the projection data P violates the linear attenuation model assumed by FBP, resulting in pronounced streaking and shadowing artifacts in μ . These artifacts arise from multiple physical effects, including beam hardening, scattering, and photon starvation. Let $\mu_*(\mathbf{x})$ denote the corresponding clean CT image without metal. The objective of this study is to reconstruct $\mu_*(\mathbf{x})$ from the metal-corrupted projection data P .

We address metal artifacts in the projection domain within the NMAR framework. Let μ_{prior} denote a prior image, and let P_{prior} denote its forward projection, defined as

$$P_{\text{prior}}(\varphi, s) = \int_{\ell_{\varphi, s}} \mu_{\text{prior}}(\mathbf{x}) d\ell_{\mathbf{x}}, \quad (1)$$

where $\ell_{\varphi, s}$ represents a fan-beam ray connecting the X-ray source at angle φ to the detector position s , and $d\ell_{\mathbf{x}}$ denotes the line element along the ray. Let $D \subset \Omega$ denote the metal region in the image domain, and let $T = \{(\varphi, s) \in [0, 2\pi) \times \mathbb{R} : \int_{\ell_{\varphi, s}} \chi_D(\mathbf{x}) d\ell_{\mathbf{x}} > 0\}$ denote the metal-affected projection region (i.e., the metal trace). Here, χ_D denotes the characteristic function of D , i.e., $\chi_D(\mathbf{x}) = 1$ if $\mathbf{x} \in D$ and 0 otherwise.

Given P, P_{prior} and T , the NMAR-corrected projection data, denoted by P_{NMAR} , is obtained as

$$P_{\text{NMAR}} = L \left[\frac{P}{P_{\text{prior}}}; T \right] P_{\text{prior}}, \quad (2)$$

where $L[\cdot]$ denotes a one-dimensional linear interpolation operator applied along the detector coordinate s for each fixed projection angle φ . It replaces metal-corrupted data in the

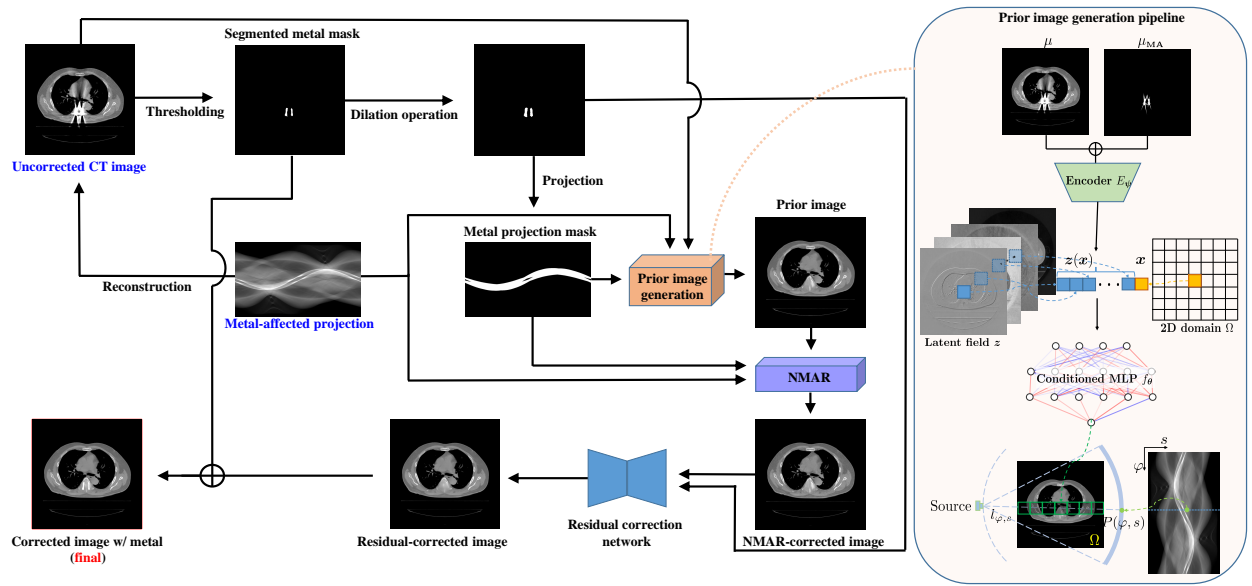


Figure 1: Schematic diagram of the MGMAR framework, which exploits metal-related information throughout the pipeline via a metal artifact-aware latent-conditioned INR for prior image generation and a metal-embedded residual learning network.

normalized projection by linearly interpolated values computed from its neighboring metal-unaffected measurements. The NMAR-corrected image is then obtained by the FBP as $\mu_{\text{NMAR}} = \mathcal{B}[P_{\text{NMAR}}]$.

The NMAR reconstruction depends heavily on the quality of the prior image μ_{prior} . Specifically, an accurate prior projection P_{prior} , obtained by forward projection of μ_{prior} , enables NMAR to compensate primarily for metal-induced corruption by interpolating the normalized data P/P_{prior} , thereby better preserving anatomical structures outside the metal region D in the NMAR-corrected image μ_{NMAR} . In contrast, an inaccurate estimate of P_{prior} can induce a large interpolation error in the normalized projection,

$$\left\| L \left[\frac{P}{P_{\text{prior}}}; T \right] - 1 \right\|_T, \tag{3}$$

which can lead to severe secondary artifacts in the reconstructed image μ_{NMAR} . Here, $\|\cdot\|_T$ denotes a norm over the metal-trace region T .

In the following sections, we describe (i) an effective strategy for generating a high-quality prior image using an INR from metal-unaffected projections, and (ii) a metal-embedded residual correction method to suppress secondary artifacts in μ_{NMAR} . An overview of the MGMAR framework is illustrated in Fig. 1.

II.A. INR-based prior image generation

Given a spatial location $\mathbf{x} \in \Omega$, we aim to learn an MLP $f_{\theta} : \mathbf{x} \mapsto \mu_{\text{prior}}$ parameterized by learnable weights θ , using metal-unaffected projection measurements $P(\varphi, s)$ on $T^c := ([0, 2\pi) \times \mathbb{R}) \setminus T$. The network can be trained by minimizing the following loss:

$$\mathcal{L}_{\text{naive}}(\theta) = \mathbb{E}_{(\varphi, s) \in T^c} \left[\left\| P(\varphi, s) - \int_{\ell_{\varphi, s}} f_{\theta}(\mathbf{x}) d\ell_{\mathbf{x}} \right\|^2 \right]. \quad (4)$$

However, despite the reconstruction potential of INRs for the ill-posed problem, directly optimizing (4) can become unstable when metal-unaffected measurements are severely limited by large and multiple metallic implants. Iteratively updating the weights from random initialization often yields sub-optimal reconstructions that fluctuate across initializations and requires substantial computational cost (see Fig. 2).

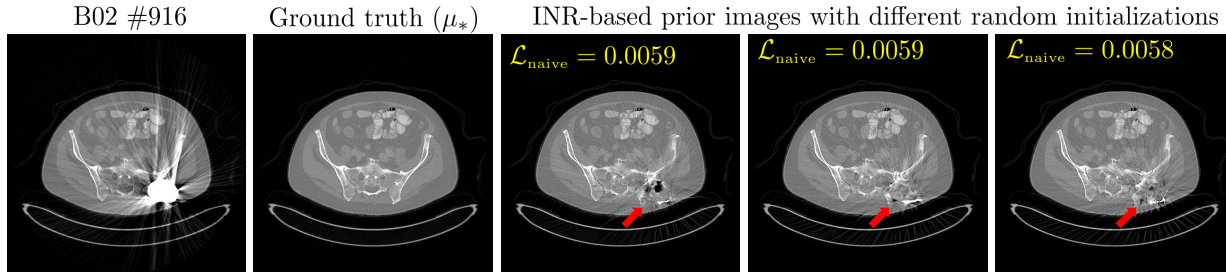


Figure 2: Prior images obtained by an INR with different random initializations. Given the projection data P from a validation case (B02 #916), the INR is optimized by minimizing the naive loss $\mathcal{L}_{\text{naive}}$ for 10,000 iterations (WW/WL = 1500/ - 250 HU for CT images). Although the final loss values are similar, the resulting reconstructions differ substantially.

II.A.1. A data-driven weight initialization strategy

To address this problem, we introduce a data-driven weight initialization that embeds prior knowledge into the MLP weights and serves as a learned initialization instead of random initialization. The initialization is obtained by pretraining a conditioned INR on a paired training dataset, where the conditioning is provided by an artifact-aware representation extracted by an encoder. Specifically, let $E_{\psi} : \mu \mapsto \mathbf{z}$ be a convolutional encoder parameterized by ψ , which takes a two-channel input $\mu := (\mu, \mu_{\text{MA}})$ and outputs an m -channel latent field $\mathbf{z} : \Omega \rightarrow \mathbb{R}^m$. Here, μ_{MA} denotes a metal-artifact image designed to emphasize metallic structures and their associated globally distributed artifact patterns. It serves as an estimate of the quantity $\mu_{\text{MA}}^* := \mu - \mu_*$. Since μ_* is unavailable during inference, we construct μ_{MA} using

the measured projection data P through a simple recursive procedure described later.

We pretrain the conditioned INR by jointly learning $(\boldsymbol{\theta}, \boldsymbol{\psi})$ from the paired training dataset $\mathcal{S}_{\text{init}} = \{(\boldsymbol{\mu}^i, \mu_*^i)\}_{i=1}^N$ via

$$\mathcal{L}_{\text{init}}(\boldsymbol{\theta}, \boldsymbol{\psi}; \mathcal{S}_{\text{init}}) = \frac{1}{N} \sum_{i=1}^N \mathbb{E}_{\mathbf{x} \in \Omega} [|f_{\boldsymbol{\theta}}(\mathbf{x}, E_{\boldsymbol{\psi}}(\boldsymbol{\mu}^i)(\mathbf{x})) - \mu_*^i(\mathbf{x})|] \quad (5)$$

Recursive construction of metal-artifact image μ_{MA} . We estimate μ_{MA}^* in a recursive manner. First, we set the initial estimate $\mu_{\text{MA}}^{(0)}$ as

$$\mu_{\text{MA}}^{(0)} := \mathcal{B}[\chi_T P],$$

where χ_T is the metal projection mask. We then update $\mu_{\text{MA}}^{(k)}$ by the recursion

$$\mu_{\text{MA}}^{(k+1)} := \mathcal{B}\left[P - P_{\text{NMAR}}^{(k)}\right], \quad k = 0, 1, \dots, K-1,$$

where $P_{\text{NMAR}}^{(k)}$ is the NMAR-corrected projection computed using a prior projection $P_{\text{prior}}^{(k)}$ as

$$P_{\text{NMAR}}^{(k)} = L \left[\frac{P}{P_{\text{prior}}^{(k)}}; T \right] P_{\text{prior}}^{(k)}. \quad (6)$$

The prior projection $P_{\text{prior}}^{(k)}$ is obtained from the conditioned INR as

$$P_{\text{prior}}^{(k)}(\varphi, s) = \int_{\ell_{\varphi, s}} f_{\boldsymbol{\theta}^{(k)}}(\mathbf{x}, \mathbf{z}^{(k)}(\mathbf{x})) d\ell_{\mathbf{x}},$$

where $\mathbf{z}^{(k)}(\mathbf{x}) = E_{\boldsymbol{\psi}^{(k)}}(\boldsymbol{\mu}^{(k)})(\mathbf{x})$ and $\boldsymbol{\mu}^{(k)} := (\mu, \mu_{\text{MA}}^{(k)})$. In each recursion step, the weights $(\boldsymbol{\theta}^{(k)}, \boldsymbol{\psi}^{(k)})$ are pretrained by minimizing $\mathcal{L}_{\text{init}}$ in (5) on a training set constructed using the current artifact estimate, denoted by $\mathcal{S}_{\text{init}}^{(k)} = \{(\boldsymbol{\mu}^{i,(k)}, \mu_*^i)\}_{i=1}^N$, where $\boldsymbol{\mu}^{i,(k)} := (\mu^i, \mu_{\text{MA}}^{i,(k)})$. Finally, we set $\mu_{\text{MA}} := \mu_{\text{MA}}^{(K)}$ for a suitably chosen K . Fig. 3 shows an example of the constructed metal-artifact images $\mu_{\text{MA}}^{(k)}$ at successive recursion steps ($k = 0, 1, 2$). As the recursion proceeds, $\mu_{\text{MA}}^{(k)}$ progressively approaches the target artifact-only image μ_{MA}^* in terms of RMSE.

II.A.2. Measurement-specific adaptation of the INR

Starting from the data-driven initialization $\boldsymbol{\theta}_0 := \boldsymbol{\theta}^{(K)}$ obtained in (5), we further adapt the INR to each measurement P by enforcing data fidelity on the metal-unaffected region T^c ,

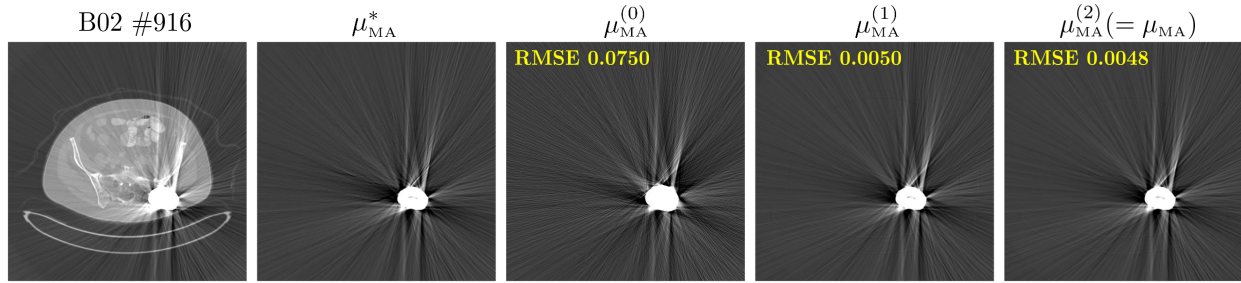


Figure 3: Constructed metal-artifact images $\mu_{\text{MA}}^{(k)}$ across recursion steps ($k = 0, 1, 2$). The RMSE with respect to the target μ_{MA}^* is reported at the top of each panel (WW/WL = 2000/ - 500).

Algorithm 1: Prior image generation with data-driven initialization for NMAR

Require: Metal-corrupted projection $P(\varphi, s)$; metal trace T ; metal trace mask χ_T ; FBP reconstruction $\mu = \mathcal{B}[P]$; pretrained encoders $\{E_{\psi^{(k)}}\}_{k=0}^K$; pretrained INRs $\{f_{\theta^{(k)}}\}_{k=0}^K$; recursion steps K ; refinement iterations N_{iter} .

Ensure: Prior image μ_{prior} .

- 1: **(Construction of μ_{MA})** $\mu_{\text{MA}}^{(0)} \leftarrow \mathcal{B}[\chi_T P]$.
 - 2: **for** $k = 0, 1, \dots, K - 1$ **do**
 - 3: $\boldsymbol{\mu}^{(k)} \leftarrow (\mu, \mu_{\text{MA}}^{(k)}), \quad \mathbf{z}^{(k)} \leftarrow E_{\psi^{(k)}}(\boldsymbol{\mu}^{(k)})$.
 - 4: $P_{\text{prior}}^{(k)}(\varphi, s) \leftarrow \int_{\ell_{\varphi, s}} f_{\theta^{(k)}}(\mathbf{x}, \mathbf{z}^{(k)}(\mathbf{x})) d\ell_{\mathbf{x}}, \quad \forall (\varphi, s) \in [0, 2\pi) \times \mathbb{R}$.
 - 5: $P_{\text{NMAR}}^{(k)} \leftarrow L \left[\frac{P}{P_{\text{prior}}^{(k)}}; T \right] P_{\text{prior}}^{(k)}$.
 - 6: $\mu_{\text{MA}}^{(k+1)} \leftarrow \mathcal{B} \left[P - P_{\text{NMAR}}^{(k)} \right]$.
 - 7: **end for**
 - 8: $\mu_{\text{MA}} \leftarrow \mu_{\text{MA}}^{(K)}, \quad \boldsymbol{\mu} \leftarrow (\mu, \mu_{\text{MA}}), \quad \mathbf{z} \leftarrow E_{\psi^{(K)}}(\boldsymbol{\mu}), \quad \boldsymbol{\theta}_0 \leftarrow \boldsymbol{\theta}^{(K)}$.
 - 9: **(Refinement of INR on T^c)** $\boldsymbol{\theta} \leftarrow \text{OPT}(\boldsymbol{\theta}_0, \mathcal{L}_{\text{fid}}(\boldsymbol{\theta}), N_{\text{iter}})$.
 - 10: $\mu_{\text{prior}}(\mathbf{x}) \leftarrow f_{\boldsymbol{\theta}}(\mathbf{x}, \mathbf{z}(\mathbf{x})), \quad \forall \mathbf{x} \in \Omega$.
 - 11: **return** μ_{prior} .
-

subject to structural constraints derived from the initial weight $\boldsymbol{\theta}_0$. Specifically, for a given encoder input $\boldsymbol{\mu} = (\mu, \mu_{\text{MA}})$, we refine $f_{\boldsymbol{\theta}}$ by minimizing

$$\mathcal{L}_{\text{fid}}(\boldsymbol{\theta}) = \mathbb{E}_{(\varphi, s) \in T^c} \left[\left\| P(\varphi, s) - \int_{\ell_{\varphi, s}} f_{\boldsymbol{\theta}}(\mathbf{x}, \mathbf{z}(\mathbf{x})) d\ell_{\mathbf{x}} \right\| \right] + \lambda \mathbb{E}_{\mathbf{x} \in \Omega} [|f_{\boldsymbol{\theta}}(\mathbf{x}, \mathbf{z}(\mathbf{x})) - f_{\boldsymbol{\theta}_0}(\mathbf{x}, \mathbf{z}(\mathbf{x}))|], \quad (7)$$

where $\mathbf{z} = E_{\psi^{(K)}}(\boldsymbol{\mu})$ is the latent field extracted by the pretrained encoder in (5), and $\lambda > 0$ is the regularization parameter. Finally, we obtain the prior image by evaluating the refined INR at each spatial location, i.e., $\mu_{\text{prior}}(\mathbf{x}) := f_{\boldsymbol{\theta}}(\mathbf{x}, \mathbf{z}(\mathbf{x}))$ for all $\mathbf{x} \in \Omega$. The overall inference procedure for generating the prior image using the data-driven initialization is summarized in Algorithm 1.

II.B. Metal-embedded residual learning

To suppress the remaining artifacts in the NMAR-corrected image μ_{NMAR} , we adopt an image-domain residual learning strategy. We denote the residual artifacts by $r = \mu_{\text{NMAR}} - \mu_*$. Motivated by the observation that these artifacts are prominent around metallic implants, we condition the residual network on metal features. Specifically, let $G_\phi : (\mu_{\text{NMAR}}; \chi_D) \mapsto r$ be a residual network parameterized by ϕ , where χ_D denotes the metal mask corresponding to the given reconstruction μ_{NMAR} . We train G_ϕ on the paired dataset $\mathcal{S}_{\text{res}} = \{(\mu_{\text{NMAR}}^i, r^i)\}_{i=1}^N$ by minimizing

$$\mathcal{L}_{\text{res}}(\phi; \mathcal{S}_{\text{res}}) = \frac{1}{N} \sum_{i=1}^N \mathbb{E}_{\mathbf{x} \in \Omega} [|G_\phi(\mu_{\text{NMAR}}^i; \chi_D^i)(\mathbf{x}) - r^i(\mathbf{x})|]. \quad (8)$$

Here, the metal mask χ_D^i is fed into G_ϕ through an AdaIN-based conditioning mechanism^{44,45}.

AdaIN-based metal conditioning. We first assume that G_ϕ is implemented as a multi-scale convolutional encoder-decoder. Let $\mathbf{h} : \Omega \rightarrow \mathbb{R}^{J_{\mathbf{h}}}$ denote an intermediate feature field generated within G_ϕ during the forward pass, where $\mathbf{h}(\mathbf{x}) = [h_1(\mathbf{x}), \dots, h_{J_{\mathbf{h}}}(\mathbf{x})]^\top$ and $h_j : \Omega \rightarrow \mathbb{R}$ denotes its j -th channel. Here, $J_{\mathbf{h}}$ is the number of feature channels of \mathbf{h} . AdaIN modulates each channel by matching its spatial mean and standard deviation to target statistics predicted from the metal mask χ_D . Formally, given \mathbf{h} , the AdaIN-modulated channel-wise feature field is defined by

$$\Gamma(h_j; \alpha_j, \beta_j)(\mathbf{x}) = \frac{\beta_j}{\sigma_{\mathbf{x} \in \Omega}[h_j]} (h_j(\mathbf{x}) - \mathbb{E}_{\mathbf{x} \in \Omega}[h_j(\mathbf{x})] \mathbf{1}(\mathbf{x})) + \alpha_j \mathbf{1}(\mathbf{x}), \quad (9)$$

where $\mathbf{1} : \Omega \rightarrow \mathbb{R}$ denotes the constant-one function, and α_j and β_j are channel-wise affine parameters. These parameters are produced by a network F_ζ conditioned on the metal mask χ_D :

$$F_\zeta : \chi_D \mapsto \{(\alpha_j, \beta_j)\}_{j=1}^{J_{\mathbf{h}}}. \quad (10)$$

The network F_ζ is jointly learned with G_ϕ , enabling metal-dependent modulation of multi-scale features. A schematic of the residual network with AdaIN-based conditioning is provided in the AAPM-MAR benchmark paper⁴¹ (Fig. 5(b)), where an earlier version of our MAR method submitted to the AAPM-MAR challenge is summarized.

III. Experiments

III.A. Experimental Settings

Datasets. We evaluate our method on the public AAPM-MAR benchmark dataset. The benchmark contains 14,000 simulated 2D CT datasets generated using a hybrid CT simulation pipeline, which combines real clinical head and body CT images with virtual fractal-shaped metal objects inserted at random locations in soft tissue or bone. The simulated metal materials include amalgam, stainless steel, copper, cobalt, and titanium. Each dataset provides paired data in both projection and image domains, including sinograms with and without metal, FBP-reconstructed images with and without metal artifacts, and a binary metal mask. The reconstructed images are provided on a 512×512 grid with a field of view (FOV) of 400 mm for body data and 220.16 mm for head data. We split the 14,000 simulated datasets into training and validation sets with a 9:1 ratio, resulting in 12,600 training datasets and 1,400 validation datasets.

For testing, the benchmark provides 29 clinical metal-corrupted datasets in both sinogram and image domains, without ground-truth sinograms or images available. These datasets cover a wide range of clinically relevant scenarios, including small implants (e.g., surgical clips, fiducial markers, and dental fillings), medium-sized implants (e.g., pacemakers and spinal fixation devices), and large joint replacements (e.g., shoulder and hip prostheses).

Metrics and Baselines. For the validation datasets, where artifact-free references are available, we compute conventional image-quality metrics including RMSE, PSNR, and SSIM. For the test datasets, evaluation follows the AAPM-MAR benchmark protocol using eight clinically relevant scoring metrics: CT number (CTN) accuracy, noise, image sharpness, streak amplitude, structural integrity (SSIM), metal integrity, bone integrity, and proton beam range (PBR) influence. Detailed definitions of these metrics are provided in^{41,46}. Each metric is normalized to a score in $[0, 4]$, where 0 corresponds to the ground-truth reference and 4 corresponds to the uncorrected image. The final benchmark score is computed as the average of the eight normalized metrics across all 29 test cases. All validation metrics and benchmark scores are computed using the official Python code released in the challenge’s GitHub repository⁴⁷.

We compare our method with representative baselines reported in the benchmark paper⁴¹, including the top three approaches from the final leaderboard and the conventional NMAR method⁸. The first-ranked method adopts a dual-learning framework that enforces cycle consistency between projections and reconstructed images while explicitly modeling physical effects such as photon starvation, beam hardening, noise, and scatter. It employs multiple network architectures, including U-Net, CNN, and MLP, within the framework. The third-ranked method employs a dual-domain framework that first performs metal segmentation in both the projection and image domains, and then alternates between sinogram inpainting and image-domain artifact reduction to progressively refine the reconstructed image. It employs a Swin Transformer-based U-Net and a ResNet within the framework. The second-ranked method corresponds to our preliminary submission. In this work, we further improve performance by introducing the proposed data-driven prior image generation and simplifying the overall pipeline by removing a redundant NMAR step previously applied at the end of the procedure, while keeping the same metal segmentation protocol used in our prior work.

Implementation details. The implementation is performed using the PyTorch framework⁴⁸. The MLP network f_{θ} consists of 4 hidden fully connected layers, each with 256 units and ReLU activation⁴⁹. For the conditioning encoder E_{ψ} , we adopt an EDSR-baseline architecture⁵⁰ with 16 residual blocks and 64 feature channels. We use a no-upsampling configuration so that the encoder produces a latent feature map at the same spatial resolution as the input image. This enables pixel-wise conditioning of the INR, i.e., $\mathbf{z}(\mathbf{x}) = E_{\psi}(\boldsymbol{\mu})(\mathbf{x})$.

At test time, the artifact image μ_{MA} is constructed via the recursive procedure with $K = 2$ recursion steps (Algorithm 1). We pretrain each stage-specific conditioned INR $(E_{\psi^{(k)}}, f_{\theta^{(k)}})$, for $k = 0, 1, \dots, K$, on the paired dataset $\mathcal{S}_{\text{init}}^{(k)}$ by minimizing $\mathcal{L}_{\text{cond}}$ in (5) using a learning rate of 10^{-4} for 1,000 epochs. For each measurement P , the globally initialized weight $\boldsymbol{\theta}_0 = \boldsymbol{\theta}^{(K)}$ is further optimized by solving the data-fidelity problem in (7) with a learning rate of 5×10^{-6} for $N_{\text{iter}} = 1000$ iterations and the regularization parameter $\lambda = 10$. During this refinement, the encoder is fixed to $E_{\psi^{(K)}}$.

The residual network G_{ϕ} is implemented as a multi-scale convolutional encoder–decoder based on deep convolutional framelets⁵¹. At each scale, the network consists of two con-

secutive 4×4 convolutional layers, each followed by an AdaIN layer and a LeakyReLU activation⁵². It employs 2-D Haar wavelet decomposition and reconstruction⁵³ to perform downsampling and upsampling, respectively.

The AdaIN parameter prediction network F_ζ follows the branch network architecture⁵⁴. It takes the conditioning metal mask χ_D as input and jointly predicts the affine parameters for all AdaIN layers in G_ϕ in a single forward pass. Specifically, F_ζ consists of a shared convolutional trunk with 4 convolution layers, followed by a flatten operation and two fully connected layers. From the final latent vector, F_ζ employs parallel output heads to produce the channel-wise shift and scale parameters $\{(\alpha_j, \beta_j)\}_{j=1}^{J_{\mathbf{h}}}$ for each AdaIN-modulated feature field \mathbf{h} in G_ϕ , yielding an output of dimension $2J_{\mathbf{h}}$ per feature field.

The residual learning is performed in a patch-by-patch manner. In each iteration, we randomly extract 16 paired patches of size 128×128 from the NMAR-corrected image μ_{NMAR} and the corresponding metal mask χ_D . These patch pairs are used to train G_ϕ with a learning rate of 10^{-4} for 200 epochs.

Finally, to estimate the metal region D in the uncorrected CT image μ , we employ a simple thresholding method. Specifically, a threshold value of 0.12 is used for the validation datasets, while the metal masks for the test datasets are further manually refined. Before forward projection to compute the metal trace, the estimated metal mask is dilated using a disk-shaped structuring element of radius 2⁵⁵.

III.B. Results

Effect of data-driven initialization for prior image generation. Fig. 4 compares prior images obtained by INRs initialized with random, meta, and proposed data-driven weights across the number of iterations (N_{iter}). In this study, the meta initialization is obtained by pretraining the network on 5,000 ground-truth projection datasets randomly sampled from the training set, using a learning rate of 5×10^{-4} . As shown in Fig. 4, compared to random and meta initializations, the proposed data-driven initialization produces high-quality prior reconstructions even without network training (i.e., $N_{\text{iter}} = 0$), achieving near-optimal RMSE, PSNR, and SSIM while preserving anatomical structures in metal-affected regions with minimal degradation. Subsequent iterations lead to gradual improvements in

prior quality, with performance saturating around $N_{\text{iter}} = 1000$.

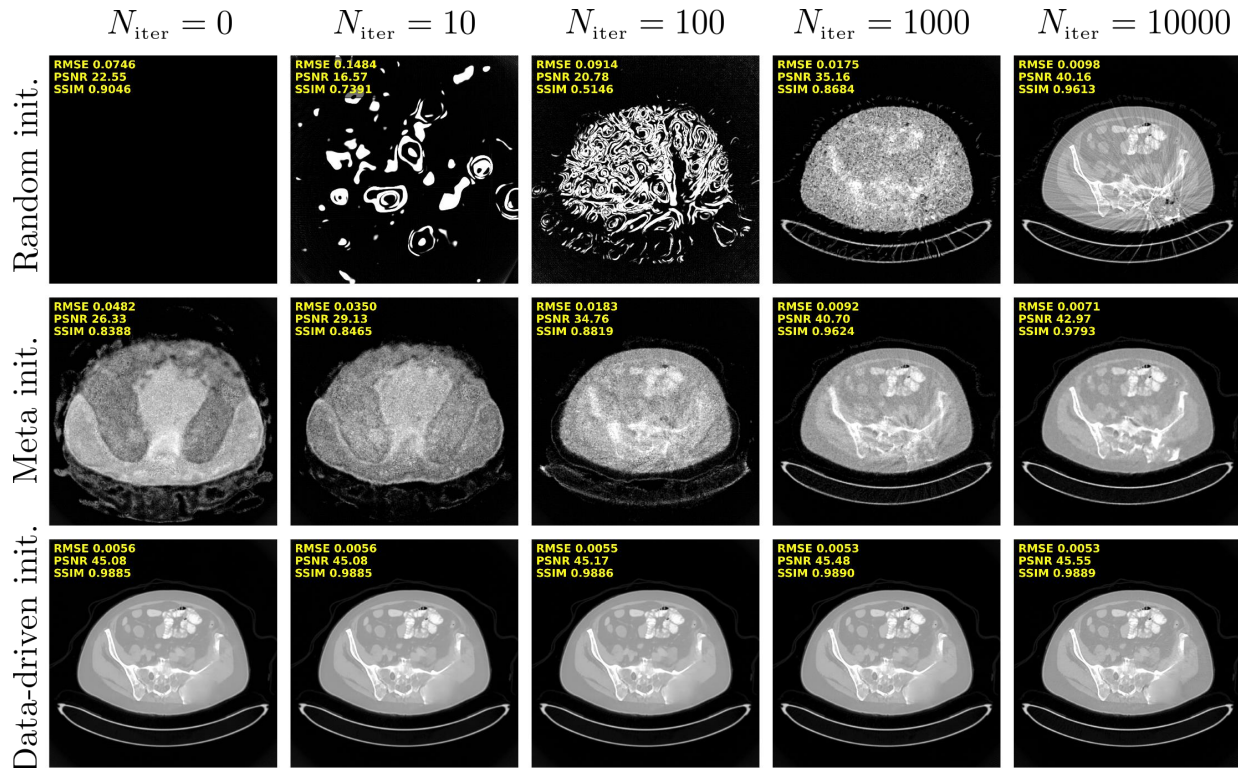


Figure 4: Comparison of prior images obtained by INRs initialized with random, meta, and the proposed data-driven weights across the number of iterations N_{iter} (WW/WL = 1500/-250 HU for CT images).

Effects of NMAR and residual correction. Fig. 5 illustrates the impact of NMAR and residual correction. While the INR-based prior image exhibits high-quality reconstruction, it fails to fully preserve structural sharpness, resulting in slightly oversmoothed boundaries (yellow arrows). The NMAR-corrected image better preserves the overall structural sharpness, as it modifies only the metal-trace region of the measured projection data while retaining the original measurements elsewhere. However, it suffers from secondary artifacts caused by inaccurate interpolation, particularly in the vicinity of metallic objects (red arrows). The residual learning effectively suppresses these secondary artifacts and mitigates the additional streaking artifacts (blue arrows) in the NMAR-corrected image. For quantitative analysis, RMSE is computed within the blue rectangular region marked in the figure. The RMSE decreases from 0.0021 to 0.0016.

Table 1 summarizes the quantitative performance of each stage (i.e., prior-image gener-

	RMSE ↓	PSNR ↑	SSIM ↑	Runtime (s)
Uncorrected	0.0143 ± 0.0059	37.44 ± 3.01	0.9307 ± 0.0295	-
Prior image				
$N_{\text{iter}} = 0$	0.0045 ± 0.0029	47.82 ± 3.56	0.9857 ± 0.0161	6
$N_{\text{iter}} = 1000$	0.0042 ± 0.0024	48.36 ± 3.52	0.9860 ± 0.0162	41
NMAR-corrected	0.0037 ± 0.0017	49.24 ± 3.43	0.9869 ± 0.0113	2
Residual-corrected	0.0032 ± 0.0016	50.74 ± 3.60	0.9904 ± 0.0097	1

Table 1: Quantitative results of each stage on the validation set, along with the average runtime per case. The quantitative results are reported as mean \pm standard deviation. ation, NMAR, and residual correction) on the entire validation set, along with the average runtime per case. All runtimes are measured on a system equipped with an Intel Xeon Gold 6226R CPU (2.90 GHz) and an NVIDIA RTX 3090 GPU (24 GB). Each stage consistently improves RMSE, PSNR, and SSIM. In terms of computational cost, prior-image generation dominates the total runtime, as it involves the recursive construction of the metal-artifact image μ_{MA} and iterative refinement of the MLP network f_{θ} (i.e., $N_{\text{iter}} = 1000$). In contrast, NMAR and residual correction introduce only minor overhead.

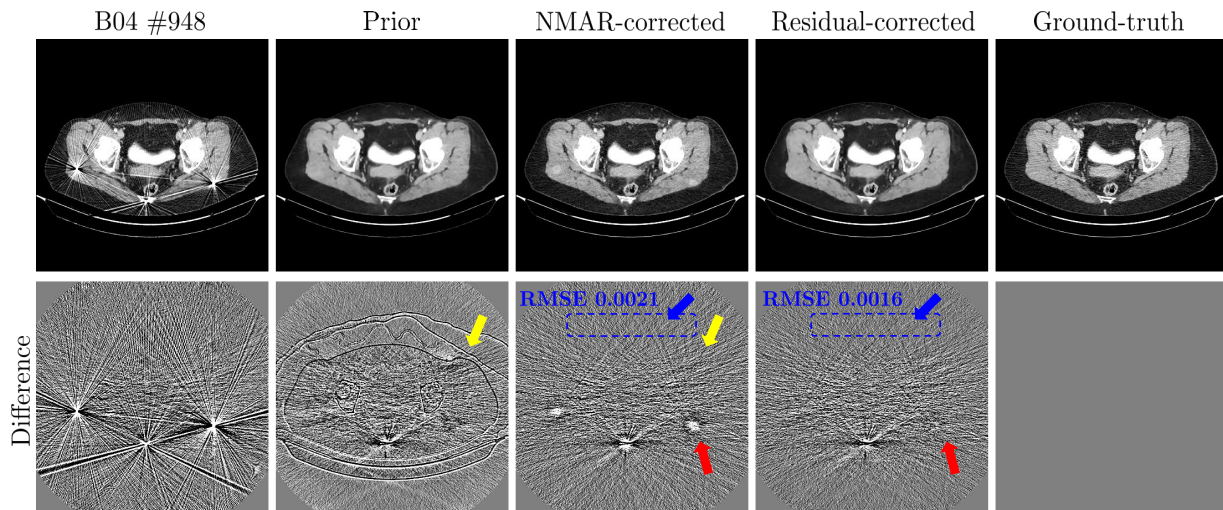


Figure 5: Visual comparison of prior, NMAR-corrected, and residual-corrected images on a validation case (B04 #948) (WW/WL = 300/0 HU for CT images, WW/WL = 50/0 HU for difference images).

Ablation study. Fig. 6 investigates the effect of incorporating the metal-artifact image μ_{MA} into the encoder input for prior image generation. The second and third panels show prior images produced by the pretrained network f_{θ_0} under two pretraining configurations:

the data-driven initial weight θ_0 is obtained from a model whose encoder is trained with μ as a single-channel input, and from a model whose encoder is trained with the two-channel input (μ, μ_{MA}) , respectively. As shown in Fig. 6, incorporating μ_{MA} substantially improves prior estimation under severe metal corruption. It better preserves anatomical structures while suppressing streaking and shadowing artifacts (red arrows).

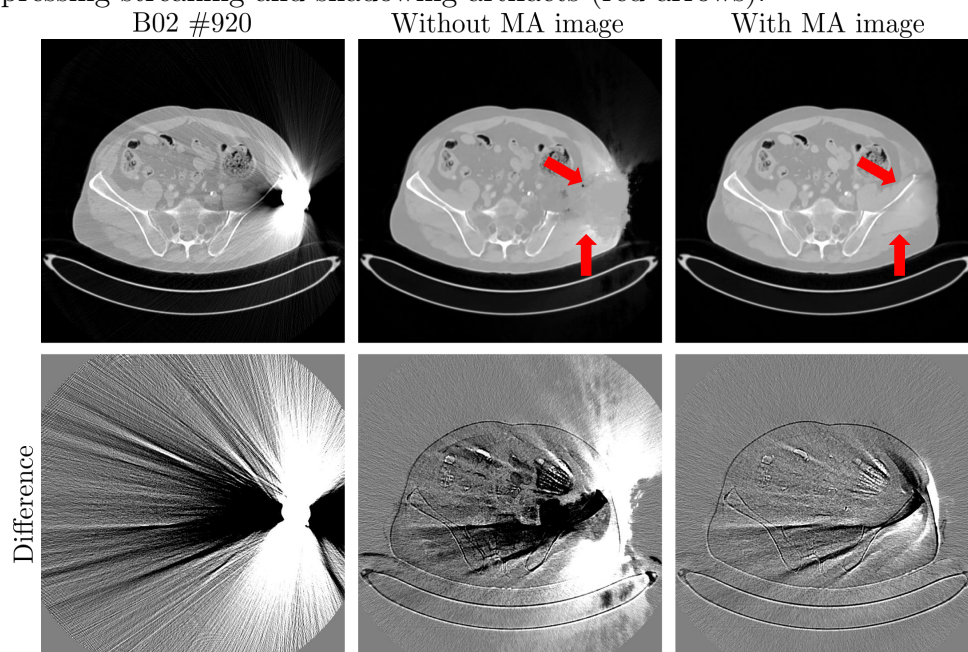


Figure 6: Effect of the metal-artifact image μ_{MA} for prior image generation (WW/WL = 1500/-250 HU for CT images, WW/WL = 200/0 HU for difference images).

We also examine the impact of metal conditioning in the residual learning stage. The corresponding results for two different validation cases are shown in Fig. 7. For each case, the middle and right panels show residual-corrected results obtained by the pretrained network without and with AdaIN-based metal conditioning, respectively. Without metal conditioning, the residual network tends to introduce unintended distortions of anatomical structures (red arrows). In contrast, metal conditioning guides the network to focus the correction on metal-dependent secondary artifacts while better preserving other anatomical details.

Table 2 summarizes the quantitative results of the ablation study on the entire validation set. Incorporating the metal-artifact image μ_{MA} into the encoder input yields a significant improvement in prior image generation, consistently reducing RMSE and increasing PSNR and SSIM. In contrast, the gain from metal conditioning in the residual learning stage is relatively modest. This may be because the residual artifacts remaining after NMAR are

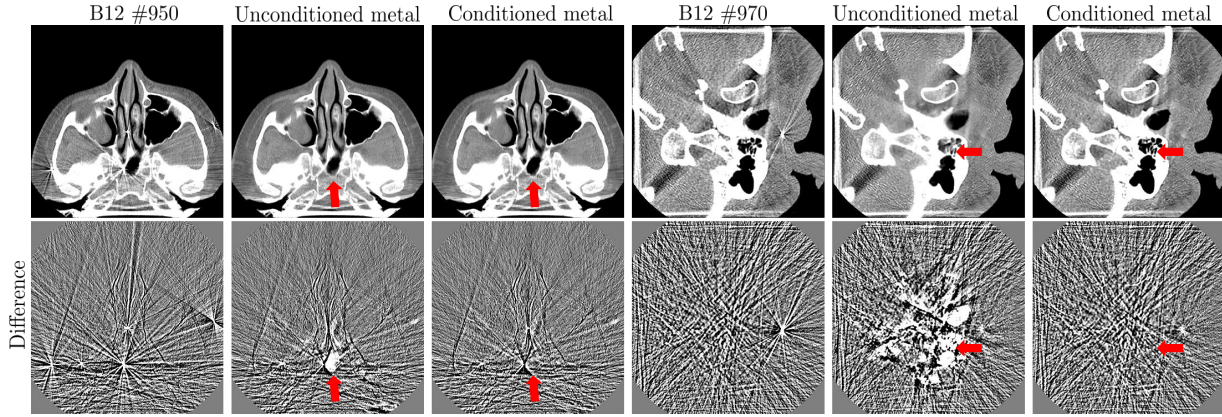


Figure 7: Effect of metal conditioning in residual learning (WW/WL = 1000/0 HU for CT images, WW/WL = 200/0 HU for difference images).

	RMSE ↓	PSNR ↑	SSIM ↑
Data-driven initialization			
without μ_{MA}	0.0053 ± 0.0031	46.46 ± 3.52	0.9835 ± 0.0179
with μ_{MA}	0.0045 ± 0.0029	47.82 ± 3.56	0.9857 ± 0.0161
Residual correction			
without χ_D	0.0033 ± 0.0017	50.67 ± 3.64	0.9903 ± 0.0102
with χ_D	0.0032 ± 0.0016	50.74 ± 3.60	0.9904 ± 0.0097

Table 2: Ablation study on the effects of the metal-artifact image μ_{MA} in prior image generation and metal conditioning in the residual learning stage. The quantitative results are reported on the validation set.

small in magnitude, leaving limited room for further improvement in quantitative metrics.

Results on the test dataset. Table 3 reports the final benchmark score and the average value of each evaluation metric over all 29 test cases for the top three methods (ranked first, second, and third) in the AAPM-MAR challenge, conventional NMAR, and MGMAR. MGMAR achieves the best final score of 0.89 (or 0.8890 when rounded to four decimal places) among the compared MAR approaches. It attains the best performance on four evaluation metrics: CTN accuracy, noise, SSIM, and PBR influence. Compared to our preliminary submission (the second-ranked method), the enhanced version of our method improves most metrics, except for sharpness and metal integrity. The reduction in sharpness is attributed to the final residual learning stage, which suppresses secondary artifacts including streaks and noise but may also attenuate fine structures, resulting in a lower sharpness score. Moreover, although the same metal mask is used as in the preliminary method, the metal integrity score

Ranking	1	2	3	NMAR	Proposed
Final score	0.96	0.98	0.99	1.82	0.89
CTN	0.74	0.81	0.82	2.03	0.72
Noise	0.01	0.19	0.01	1.06	0.01
Sharpness	0.72	0.52	0.54	0.58	0.73
Streak	1.29	1.65	1.48	1.99	1.33
SSIM	0.75	0.95	0.98	2.03	0.72
Metal integrity	1.46	1.09	0.96	2.06	1.13
Bone integrity	0.89	0.99	1.09	2.05	0.93
PBR	1.79	1.62	2.03	2.76	1.55

Table 3: Final benchmark score and average values of each evaluation metric over all 29 test cases for the selected methods ranked first, second, and third in the AAPM-MAR challenge, traditional NMAR, and MGMAR.

differs (1.09 for the previous version vs. 1.13 for the enhanced version). This is because the benchmark evaluates metal integrity based on voxels whose intensities exceed a predefined threshold. We observed that, in many cases, high-intensity values above this threshold in non-metal regions are counted as metal, thereby affecting the reported metal integrity.

Fig. 8 compares corrected images obtained by MGMAR and an earlier version of our method on representative test cases, including head, thorax, and pelvis. Compared to the previous version, MGMAR more effectively suppresses streaking and shadowing artifacts near metallic objects (red arrows) and reduces noise in homogeneous tissue regions (yellow arrows). However, it attenuates fine structural details, leading to reduced sharpness in the reconstructed image (green arrows). The corresponding ground-truth images are visualized in the benchmark paper⁴¹. For a qualitative comparison, we adopt the same window setting as used in the benchmark paper. The final reconstructed CT images obtained by MGMAR (raw files) for all test cases, along with their corresponding evaluation metric scores, are provided in the supplementary materials.

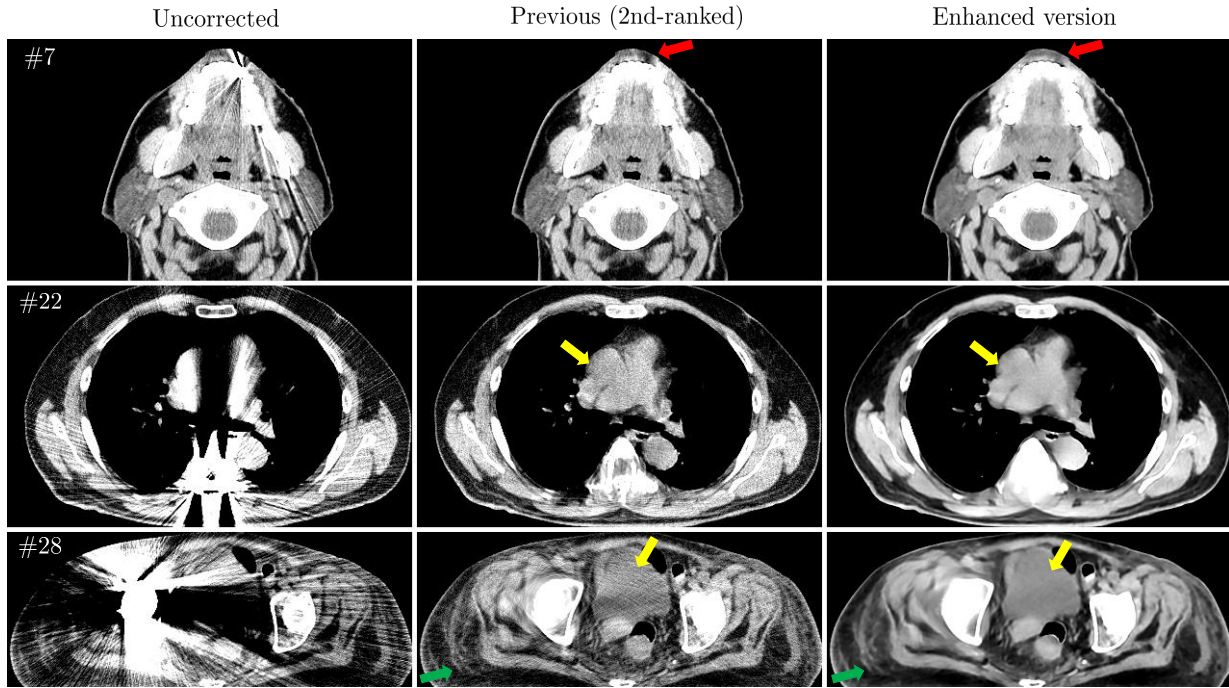


Figure 8: Visual comparison of corrected images obtained by MGMAR and an earlier version of our method (ranked second in the AAPM-MAR challenge) for head (first row), thorax (second row), and pelvis (third row) test cases (WW/WL = 200/0 HU).

IV. Discussion and Conclusion

In this work, we present MGMAR, a metal-guided MAR framework that explicitly exploits metal-related information throughout the pipeline. Specifically, we design an artifact-aware latent conditioning strategy for prior-image generation. This design enables the latent field (i.e., $z = E_{\psi}(\mu)$) to capture metal-dependent global artifact patterns (e.g., streaking and shadowing), thereby improving the stability and fidelity of the conditioned INR under severe metal corruption (Fig. 6). In addition, we incorporate explicit metal information in the residual correction stage by conditioning the metal mask into the residual network through an AdaIN-based modulation mechanism. This metal conditioning encourages the residual network to focus its capacity on metal-dependent secondary artifacts induced by projection completion, while reducing unintended distortions in non-metal anatomical regions (Fig. 7).

We also propose a data-driven weight initialization strategy for INR-based prior-image reconstruction. Instead of relying on random initialization, we embed data-driven prior knowledge directly into the MLP parameter space by pretraining a conditioned INR on paired metal-corrupted and artifact-free CT images. This prior-embedded initialization guides the

measurement-specific refinement toward a more reliable solution manifold under severely limited metal-affected measurements, while reducing sensitivity to random initialization and accelerating convergence to a high-quality prior image (Fig. 4).

Related to prior-knowledge embedding, Shen *et al.*³⁵ leverage an additional CT scan of the same patient as prior information, whose pretrained weights are used to initialize the MLP for sparse-view CT reconstruction. While this strategy can improve reconstruction quality, its applicability may be limited in general clinical workflows where sequential CT scans of the same patient are not routinely available. Meta-learning frameworks embed prior knowledge into the MLP by pretraining on samples from the target domain. Such strategies have been explored for neural radiance fields⁴³ and CBCT reconstruction⁵⁶. Compared to random initialization, meta-learned initializations can improve optimization stability and reduce training time; however, recovering fine anatomical details may still require substantial computation, and the resulting reconstructions can remain suboptimal under severe metal corruption (Fig. 4).

The validation results demonstrate that each component of the proposed pipeline contributes consistently to artifact suppression and image-quality improvement (Table 1) in terms of RMSE, PSNR, and SSIM. The prior-image generation stage provides a substantial reduction in reconstruction error, indicating that the conditioned INR yields an effective estimate even under severe metal corruption. The subsequent NMAR step further improves the reconstruction by restricting modifications to the metal-trace region, which helps preserve structural sharpness that is not fully recovered in the INR-based prior image. Finally, the residual correction stage provides an additional improvement by removing secondary artifacts around metallic objects and reducing additional streaking artifacts, leading to the best quantitative performance on the validation set. On the clinical test set, MGMAR outperforms the baseline methods across multiple clinically relevant metrics, including CTN accuracy, noise, SSIM, and PBR influence, and achieves the best final benchmark score on the AAPM-MAR benchmark (Table 3).

The proposed data-driven initialization relies on paired training datasets with artifact-free references, which may be difficult to acquire in real clinical settings. In practice, vendor-specific, physics-based numerical simulation pipelines can be used to generate realistic training data, thereby mitigating the domain gap between training and clinical domains^{23,24,57}.

In addition, although the proposed data-driven initialization significantly reduces the computational burden compared to random and meta initializations, the overall runtime of the proposed method is still approximately 50 s per case, with the majority of the time (41 s) spent on the measurement-specific refinement. Future work will therefore focus on further accelerating the refinement stage, for example through more efficient optimization strategies, and on extending the proposed framework to real clinical workflows and more complex 3D cone-beam CT geometries.

Acknowledgment

H. S. Park and K. Jeon were supported by the National Institute for Mathematical Sciences (NIMS) grant funded by the Korean government (No. NIMS-B26A10000). H. S. Park and K. Jeon were partially supported by the National Research Foundation of Korea(NRF) grant funded by the Korea government(MSIT) (No. RS-2024-00338419).

References

- ¹ L. Gjestebj, Q. Yang, Y. Xi, H. Shan, B. Claus, Y. Jin, B. D. Man, and G. Wang, Deep learning methods for CT image-domain metal artifact reduction, in *Proceedings Volume 10391, Developments in X-Ray Tomography XI*, 2017.
 - ² M. H. Elnagar, S. Aronovich, and B. Kusnoto, Digital workflow for combined orthodontics and orthognathic surgery, *Oral and Maxillofacial Surgery Clinics* **32**, 1–14 (2020).
 - ³ R. N. Bracewell and A. C. Riddle, Inversion of fan-beam scans in radio astronomy, *Astrophysical Journal* **150**, 427–434 (1967).
 - ⁴ H. S. Park, C. M. Hyun, and J. K. Seo, Nonlinear ill-posed problem in low-dose dental cone-beam computed tomography, *IMA Journal of Applied Mathematics* **89**, 231–253 (2024).
 - ⁵ M. Abdoli, M. R. Ay, A. Ahmadian, R. A. J. O. Dierckx, and H. Zaidi, Reduction of
-

- dental filling metallic artifacts in CT-based attenuation correction of PET data using weighted virtual sinograms optimized by a genetic algorithm, *Medical Physics* **37**, 6166–6177 (2010).
- ⁶ W. A. Kalender, R. Hebel, and J. Ebersberger, Reduction of CT artifacts caused by metallic implants, *Radiology* **164**, 576–577 (1987).
 - ⁷ R. M. Lewitt and R. H. T. Bates, Image reconstruction from projections: IV. Projection completion methods (computational examples), *Optik* **50**, 269–278 (1978).
 - ⁸ E. Meyer, R. Raupach, M. Lell, B. Schmidt, and M. Kachelrieß, Normalized metal artifact reduction (NMAR) in computed tomography, *Medical Physics* **37**, 5482–5493 (2010).
 - ⁹ H. S. Park, J. K. Choi, K.-R. Park, K. S. Kim, S.-H. Lee, J. C. Ye, and J. K. Seo, Metal artifact reduction in CT by identifying missing data hidden in metals, *Journal of X-ray science and technology* **21**, 357–372 (2013).
 - ¹⁰ J. C. Roeske, C. Lund, C. A. Pelizzari, X. Pan, and A. J. Mundt, Reduction of computed tomography metal artifacts due to the Fletcher-Suit applicator in gynecology patients receiving intracavitary brachytherapy, *Brachytherapy* **2**, 207–214 (2003).
 - ¹¹ S. Zhao, D. Robeltson, G. Wang, B. Whiting, and K. Bae, X-ray CT metal artifact reduction using wavelets: an application for imaging total hip prostheses, *IEEE Transactions on Medical Imaging* **19**, 1238–1247 (2000).
 - ¹² B. D. Man, J. Nuyts, P. Dupont, G. Marchal, and P. Suetens, An iterative maximum-likelihood polychromatic algorithm for CT, *IEEE Transactions on Medical Imaging* **20**, 999–1008 (2001).
 - ¹³ I. A. Elbakri and J. A. Fessler, Statistical Image Reconstruction for Polyenergetic X-Ray Computed Tomography, *IEEE Transactions on Medical Imaging* **21**, 89–99 (2002).
 - ¹⁴ Y. Kyriakou, E. Meyer, D. Prell, and M. Kachelrieß, Empirical beam hardening correction (EBHC) for CT, *Medical physics* **37**, 5179–5187 (2010).

-
- ¹⁵ N. Menvielle, Y. Goussard, D. Orban, and G. Soulez, Reduction of Beam-Hardening Artifacts in X-Ray CT, in *IEEE Engineering in Medicine and Biology 27th Annual Conference*, pages 1865–1868, 2005.
- ¹⁶ J. A. O’Sullivan and J. Benac, Alternating minimization algorithms for transmission tomography, *IEEE Transactions on Medical Imaging* **26**, 283–297 (2007).
- ¹⁷ G. Wang, D. Snyder, J. O’Sullivan, and M. Vannier, Iterative deblurring for CT metal artifact reduction, *IEEE Transactions on Medical Imaging* **15**, 657–664 (1996).
- ¹⁸ A. Mehranian, M. R. Ay, A. Rahmim, and H. Zaidi, 3D prior image constrained projection completion for X-ray CT metal artifact reduction, *IEEE Transactions on Nuclear Science* **60**, 3318–3332 (2013).
- ¹⁹ D. Prell, Y. Kyriakou, M. Beister, and W. A. Kalender, A novel forward projection-based metal artifact reduction method for flat-detector computed tomography, *Physics in Medicine & Biology* **54**, 6575 (2009).
- ²⁰ M. Njiti, N. Osman, M. Mansor, N. Rabaiee, and M. A. Aziz, Potential of metal artifact reduction (MAR) and deep learning-based reconstruction (DLR) algorithms integration in CT metal artifact correction: A review, *Radiation Physics and Chemistry* **218**, 111541 (2024).
- ²¹ H. S. Park, D. Hwang, and J. K. Seo, Metal artifact reduction for polychromatic X-ray CT based on a beam-hardening corrector, *IEEE transactions on medical imaging* **35**, 480–487 (2015).
- ²² L. Yu, Z. Zhang, X. Li, H. Ren, W. Zhao, and L. Xing, Metal artifact reduction in 2D CT images with self-supervised cross-domain learning, *Physics in Medicine & Biology* **66**, 175003 (2021).
- ²³ Y. Zhang and H. Yu, Convolutional Neural Network Based Metal Artifact Reduction in X-Ray Computed Tomography, *IEEE Transactions on Medical Imaging* **37**, 1370–1381 (2018).
- ²⁴ H. S. Park, S. M. Lee, H. P. Kim, J. K. Seo, and Y. E. Chung, CT sinogram-consistency learning for metal-induced beam hardening correction, *Medical Physics* **45**, 5376–5384 (2018).
-

- 25 C. Peng, B. Qiu, M. Li, Y. Guan, C. Zhang, Z. Wu, and J. Zheng, Gaussian diffusion sinogram inpainting for X-ray CT metal artifact reduction, *Biomedical engineering online* **16**, 1 (2017).
- 26 Y. Zhu et al., Sinogram domain metal artifact correction of CT via deep learning, *Computers in Biology and Medicine* **155**, 106710 (2023).
- 27 W.-A. Lin, H. Liao, C. Peng, X. Sun, J. Zhang, J. Luo, R. Chellappa, and S. K. Zhou, DuDoNet: Dual Domain Network for CT Metal Artifact Reduction, in *IEEE/CVF Conference on Computer Vision and Pattern Recognition (CVPR)*, pages 10512–10521, 2019.
- 28 L. Yu, Z. Zhang, X. Li, and L. Xing, Deep Sinogram Completion With Image Prior for Metal Artifact Reduction in CT Images, *IEEE Transactions on Medical Imaging* **40**, 228–238 (2021).
- 29 B. Zhou, X. Chen, S. K. Zhou, J. S. Duncan, and C. Liu, DuDoDR-Net: Dual-domain data consistent recurrent network for simultaneous sparse view and metal artifact reduction in computed tomography, *Medical Image Analysis* **75**, 102289 (2022).
- 30 V. Sitzmann, J. Martel, A. Bergman, D. Lindell, and G. Wetzstein, Implicit neural representations with periodic activation functions, *Advances in neural information processing systems* **33**, 7462–7473 (2020).
- 31 M. Tancik, P. Srinivasan, B. Mildenhall, S. Fridovich-Keil, N. Raghavan, U. Singhal, R. Ramamoorthi, J. Barron, and R. Ng, Fourier features let networks learn high frequency functions in low dimensional domains, *Advances in Neural Information Processing Systems* **33**, 7537–7547 (2020).
- 32 B. Kim, H. Shim, and J. Baek, A streak artifact reduction algorithm in sparse-view CT using a self-supervised neural representation, *Medical physics* **49**, 7497–7515 (2022).
- 33 H. S. Park, J. K. Seo, and K. Jeon, Implicit neural representation-based method for metal-induced beam hardening artifact reduction in X-ray CT imaging, *Medical Physics* **52**, 2201–2211 (2025).

-
- ³⁴ H. S. Park and K. Jeon, Adaptive multi-resolution hash-encoding framework for INR-based dental CBCT reconstruction with truncated FOV, *Medical Physics* **53**, e70226 (2026).
- ³⁵ L. Shen, J. Pauly, and L. Xing, NeRP: implicit neural representation learning with prior embedding for sparsely sampled image reconstruction, *IEEE Transactions on Neural Networks and Learning Systems* **35**, 770–782 (2022).
- ³⁶ R. Zha, Y. Zhang, and H. Li, NAF: neural attenuation fields for sparse-view CBCT reconstruction, in *International Conference on Medical Image Computing and Computer-Assisted Intervention*, pages 442–452, Springer, 2022.
- ³⁷ Q. Wu, L. Chen, C. Wang, H. Wei, S. K. Zhou, J. Yu, and Y. Zhang, Unsupervised polychromatic neural representation for CT metal artifact reduction, *Advances in Neural Information Processing Systems* **36**, 69605–69624 (2023).
- ³⁸ Q. Wu, X. Guo, L. Chen, D. He, H. Wei, X. Wang, S. K. Zhou, Y. Zhang, J. Yu, and Y. Zhang, Unsupervised density neural representation for CT metal artifact reduction, *CoRR* (2024).
- ³⁹ Z. Chen and H. Zhang, Learning implicit fields for generative shape modeling, in *Proceedings of the IEEE/CVF conference on computer vision and pattern recognition*, pages 5939–5948, 2019.
- ⁴⁰ L. Mescheder, M. Oechsle, M. Niemeyer, S. Nowozin, and A. Geiger, Occupancy networks: Learning 3D reconstruction in function space, in *Proceedings of the IEEE/CVF conference on computer vision and pattern recognition*, pages 4460–4470, 2019.
- ⁴¹ E. Haneda et al., AAPM CT metal artifact reduction grand challenge, *Medical Physics* **52**, e70050 (2025).
- ⁴² A. Nichol, J. Achiam, and J. Schulman, On first-order meta-learning algorithms, arXiv preprint arXiv:1803.02999 (2018).
- ⁴³ M. Tancik, B. Mildenhall, T. Wang, D. Schmidt, P. P. Srinivasan, J. T. Barron, and R. Ng, Learned initializations for optimizing coordinate-based neural representations,
-

- in *Proceedings of the IEEE/CVF conference on computer vision and pattern recognition*, pages 2846–2855, 2021.
- ⁴⁴ X. Huang and S. Belongie, Arbitrary style transfer in real-time with adaptive instance normalization, in *Proceedings of the IEEE international conference on computer vision*, pages 1501–1510, 2017.
- ⁴⁵ T. Karras, S. Laine, and T. Aila, A style-based generator architecture for generative adversarial networks, in *Proceedings of the IEEE/CVF conference on computer vision and pattern recognition*, pages 4401–4410, 2019.
- ⁴⁶ N. Peters, E. Haneda, J. Zhang, G. Karageorgos, W. Xia, J. Verburg, G. Wang, H. Paganetti, and B. De Man, A hybrid training database and evaluation benchmark for assessing metal artifact reduction methods for X-ray CT imaging, *Medical Physics* **52**, e70020 (2025).
- ⁴⁷ AAPM CT Metal Artifact Reduction (CT-MAR) Grand Challenge Benchmark Tool, GitHub, https://github.com/xcist/example/tree/main/AAPM_datachallenge.
- ⁴⁸ A. Paszke, S. Gross, S. Chintala, G. Chanan, E. Yang, Z. DeVito, Z. Lin, A. Desmaison, L. Antiga, and A. Lerer, Automatic differentiation in pytorch, (2017).
- ⁴⁹ V. Nair and G. E. Hinton, Rectified linear units improve restricted boltzmann machines, in *Proceedings of the 27th International Conference on International Conference on Machine Learning*, pages 807–814, 2010.
- ⁵⁰ B. Lim, S. Son, H. Kim, S. Nah, and K. Mu Lee, Enhanced deep residual networks for single image super-resolution, in *Proceedings of the IEEE conference on computer vision and pattern recognition workshops*, pages 136–144, 2017.
- ⁵¹ J. C. Ye, Y. Han, and E. Cha, Deep Convolutional Framelets: A General Deep Learning Framework for Inverse Problems, *SIAM Journal on Imaging Sciences* **11**, 991–1048 (2018).
- ⁵² A. L. Maas et al., Rectifier nonlinearities improve neural network acoustic models, in *Proc. icml*, volume 30, page 3, Atlanta, GA, 2013.

-
- ⁵³ S. G. Mallat, A theory for multiresolution signal decomposition: the wavelet representation, *IEEE transactions on pattern analysis and machine intelligence* **11**, 674–693 (2002).
- ⁵⁴ H. S. Park, Y. J. Jeong, and K. Jeon, A Robust Multi-Domain Network for Short-Scanning Amyloid PET Image Restoration, *IEEE Transactions on Radiation and Plasma Medical Sciences* (2024).
- ⁵⁵ J. Serra, *Image analysis and mathematical morphology*, Academic Press, Inc., 1983.
- ⁵⁶ H. Shin, T. Kim, J. Lee, S. Y. Chun, S. Cho, and D. Shin, Sparse-view CBCT reconstruction using meta-learned neural attenuation field and hash-encoding regularization, *Computers in Biology and Medicine* **189**, 109900 (2025).
- ⁵⁷ H. S. Park, J. K. Seo, C. M. Hyun, S. M. Lee, and K. Jeon, A fidelity-embedded learning for metal artifact reduction in dental CBCT, *Medical physics* **49**, 5195–5205 (2022).
-